

An Adaptive Markov Random Field for Structured Compressive Sensing

Suwichaya Suwanwimolkul^{*}, Lei Zhang^{*†}, Dong Gong^{*†}, Zhen Zhang[†],
Chao Chen[‡], Damith C. Ranasinghe^{*}, and Qinfeng Shi^{*},

^{*}School of Computer Science, The University of Adelaide, Adelaide, South Australia [†]School of Computer Science and Engineering, Northwestern Polytechnical University (NPU), Xi'an, China

[‡] Department of Computer Science, The City University of New York

Abstract—Exploiting intrinsic structures in sparse signals underpins the recent progress in compressive sensing (CS). The key is to exploit such structures to achieve the two desirable properties: generality (*i.e.*, the ability to fit a wide range of signals with diverse structures) and adaptability (*i.e.*, being adaptive to a specific signal). Most existing approaches, however, often only achieve one of these two properties. In this study, we propose a novel adaptive Markov random field sparsity prior for CS, which not only is able to support a broad range of sparsity structures, but also can adapt to each sparse signal through refining the parameters of the sparsity prior with respect to the compressed measurements. To this end, the sparse signal recovery and the estimation of the parameters in the sparsity prior are jointly integrated into a unified variational optimization problem, which can be effectively solved with an alternative minimization scheme. Extensive experiments on three real-world datasets demonstrate the effectiveness of the proposed method in recovery accuracy, noise tolerance, and runtime.

I. INTRODUCTION

COMPRESSED sensing (CS) is to recover a k -sparse signal $\mathbf{x} \in \mathbb{R}^N$ from M linear measurements $\mathbf{y} = \mathbf{A}\mathbf{x}$ [1], where $\mathbf{A} \in \mathbb{R}^{M \times N}$ represents a random transformation matrix ($M < N$). By k -sparse, we refer to a signal that contains only k non-zero coefficients. CS finds most of its applications with image signals. As most of natural images are piecewise smooth, its sparse representation can be obtained through wavelet transformation. Then, this sparse signal \mathbf{x} can be compressed into a few measurements \mathbf{y} through random projection with the random transformation matrix \mathbf{A} . Recent CS algorithms focus primarily on reducing the number of measurements M . Standard state-of-the-art CS algorithms can recover a k -sparse signal \mathbf{x} from $\mathcal{O}(k \log N/k)$ noisy measurements [1].

To reduce the number of measurements required, people started to exploit the structure (*i.e.*, interdependencies or correlations) of the coefficients in a sparse signal in addition to simple sparsity [2]–[4]. In real applications, due to the complexity of the data sources and their distributions, sparse signals often exhibit diverse structures, and the structures may vary within the same dataset. Therefore, a desirable sparsity model should possess two important properties, namely, **generality** (*i.e.*, the ability to fit a wide range of signals with diverse structures) and **adaptability** (*i.e.*, being adaptive to a specific sparse signal). To this end, two dominant classes of sparsity models have been studied [3], including deterministic structured sparsity models [4]–[12] and probabilistic structured

sparsity models [13]–[17]. A brief review is in Section II.

Deterministic structured sparsity models often require prior knowledge on the geometrical structure of sparse signals. For example, group sparsity models require a prior knowledge about the group partition [5], [6]. Hierarchical sparsity models assume that the signal coefficients are organized as a tree structure [7]–[9]. In these two cases, the sample complexity can be reduced to information-theoretic optimum $\mathcal{O}(k)$ [2]. However, many signals do not follow the assumed group or tree structure. To improve the generality, one line of work exploits graph sparsity [4], [10]–[12] that represents signal structure with a graph. However, the graph components such as connected components and graph weight are customized manually. Thus, their generality comes at the cost of expensive hyperparameter tuning. Moreover, these deterministic structured sparsity models exclude all the signals that violate their geometrical structure assumptions from the feasible set. This is mainly because the restricted isometry property (RIP) [1] treats all possible k -sparse supports equally to encode k -sparse signals.

The only way to reduce sampling complexity is to limit the feasible set of k -sparse supports [2]. To avoid excluding signals and to achieve small sampling complexity, Cevher *et al.* [15] proposed the concept of Probabilistic RIP, and used Markov Random Fields (MRFs) to model structure of sparse signals. This opens up a new line of works [13]–[17], termed probabilistic structured sparsity models, which is shown to improve sparse recovery performance. However, the MRF used in these approaches is learned at the training time; thus, it lacks the adaptability to adjust to different test signals. To improve the adaptability, several recent approaches [18]–[23] exploit cluster sparsity (extension from group sparsity) where they assume that the non-zero signal coefficients are grouped as clusters. In particular, the work [22] uses MRFs and pairwise potentials to model correlation between coefficients within a cluster. However, all these methods use fixed structures. They require heavy parameters tuning, *i.e.*, the cluster size, which varies drastically on different datasets.

We present a novel graphical compressive sensing model that offers both **generality** and **adaptability**. We leverage the probabilistic MRF as the sparsity prior since it has been proven to be general [13]–[17]. Unlike existing MRF-based methods, our method uses a Bayesian principle to realize *adaptive MRF* whose *parameters* and *underlying graph* are updated according to measurements. To achieve maximal adaptability, we employ a latent variable Bayes model [24], [25] to learn

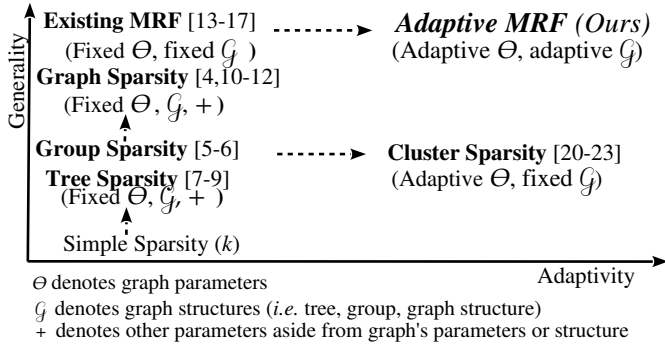
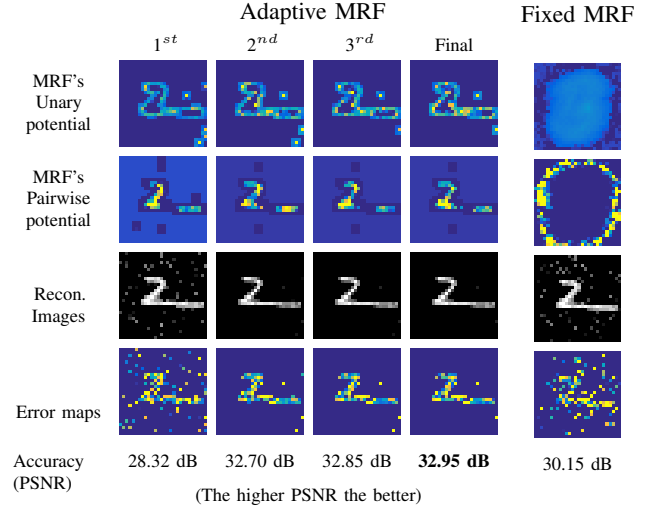


Fig. 1: Generality and adaptability in each line of work

the hyperparameters of sparse signal and estimate noise from observed measurements. This Bayes model integrates the signal recovery, support estimation, and noise estimation into a unified variational framework where all unknown variables are inferred automatically.

Generality and adaptability of the proposed adaptive MRF prior in comparison with other approaches are summarized in Figure 1. Our adaptive MRF prior possesses generality and adaptability which are inherited from the probabilistic MRF and the adaptive mechanism. Hence, unlike the cluster sparsity-based methods [18]–[23], our graphical prior can be adapted to fit any signal structure. A preliminary result of the adaptive MRF inference framework on a sample MNIST image is demonstrated in Figure 2a. The quality of the recovered image improves in each iteration, as the MRF prior being refined. The unary and pairwise potentials of the adaptive MRF are tuned to the image structure (digit 2), and they focus on the surrounding region of the drawing/stroke. This is opposite to the trained MRF that is fixed throughout signal recovery process (fixed MRF). The fixed MRF is learned from many training examples, thus, it captures a universal pattern of the training image structures. The experiment results on real-world datasets demonstrate the superiority of our model over several state-of-the-art competitors. We highlight our contributions as follows:

- 1) We propose an adaptive Markov random field (MRF) inference framework where an MRF is adapted to fit each signal structure for compressive sensing. In realizing adaptive MRF, both the MRF parameters and underlying graph are updated based on a reconstructed sparse signal. Then, our sparse signal recovery exploits the adapted MRF as a prior in signal recovery, resulting in a more accurate result. The superior performance of proposed adaptive MRF is demonstrated in Section IV-E.
- 2) Existing MRF methods [13], [14], [17] use a non-recursive two-step approach: they estimate the support with heuristic [17] or stochastic [13], [14] searching approaches and the noise and signal parameters at first; then, they estimate the sparse signal. This is time consuming. The error in the first step propagates to the second step and can not be fixed later. We propose to estimate the support, the noise and signal parameters, and the sparse signal jointly and iteratively



(a) Intermediate and final results.

(b) Final result.

Fig. 2: Comparison of the adaptive MRF and the fixed MRF on a sample MNIST data: The first (top) and the second rows include the unary potential at each image pixel and the sum of pairwise potentials of the adjacent pixels. The third and fourth rows include reconstructed images and error maps. Our adaptive MRF is much more tuned to the image structure (digit 2). However, the fixed MRF only focus on the region (the disk shape) where all digits appear.

by employing a latent variable Bayes model [24], [25] to provide a new formulation (see Eq.(12)) which brings in closed-form solutions for the noise and signal parameters and the sparse signal. Our signal recovery offers better reconstruction accuracy and runtime than using the existing heuristic [17] and the stochastic approaches [14] in the adaptive MRF framework, as illustrated in Section IV-G.

- 3) We evaluate the performance of the proposed algorithm with three benchmark datasets: i) MNIST, ii) CMU-1DB, and iii) CIFAR-10. To observe the performance in exploiting different signal structures, we study the reconstruction of sparse signals in the spatial domain and standard bases—wavelet, discrete cosine transform (DCT), and principal component analysis (PCA) bases. The results demonstrate the state-of-the-art performance in terms of accuracy in recovering the sparse signal with different structures and with moderate runtime (see Section IV-H).

II. RELATED WORK

Here we review existing deterministic and probabilistic structured sparsity models that are most relevant to our work.

A. Deterministic structured sparsity

Deterministic structured sparsity models often assume the prior knowledge on the geometric structure of sparse signals [3]. To capture the specific geometric structure, three broad classes of models are developed as follows.

Group/Block sparsity models assume that signal coeffi-

coefficients in one group/block have to be either all zero or all non-zero. This property has been enforced by l_1/l_2 norms in early works and has been extended to overlapping group-sparsity [10], [26].

Hierarchical sparsity models represent signal coefficients as trees. For example, the wavelet transform of a piecewise smooth signal often exhibits the tree structure where a zero parent node implies zero offspring nodes [7], [9]. Another example is the k -sparse rooted sub-tree model [8], where only non-zero element nodes form a sub-tree.

Graph sparsity models organize signal coefficients in a general graph, thus is able to represent various types of sparsity patterns, including the above group and hierarchical sparsity models. Initially, graph sparsity models are employed as sparsity-induced regularization to capture the overlapping-group sparsity pattern [4], [26]. Recently, approximation-tolerant methods [11], [12], [27] estimate signal supports based on the model-projection [2] where a structured sparsity prior is modelled through a graph.

However, group/block and hierarchical sparsity models only fit signals with assumed structures, thus lack generality. Graph sparsity methods have better generality; however, at the cost of extremely expensive hyperparameters tuning. These methods cannot adapt to a new signal structure. In contrast, our adaptive graphical sparsity prior enables our method to exploit a broad range of sparse signal structures without expensive hyperparameters tuning, and can adapt to a specific signal.

B. Probabilistic structured sparsity

Probabilistic structured sparsity models often assume prior knowledge about the statistical dependency of signal coefficients. Since graphical models have shown to capture complex structure of signals [7], a hidden Markov tree has been used in wavelet-based CS systems [7], [9], [28]. Inspired by the results, many works [13]–[17] use Markov random fields (MRFs), a typical graphical model, able to represent various structures probabilistically. The MRF is used to capture the structure in signal support. It is obtained through a training process and used a sparsity prior in signal recovery. With the trained MRF, the support estimation requires an exhaustive search over all possible sparsity patterns in general. To overcome the intractability of the combinatorial search, some of the previous works, *i.e.*, [15] and [16], rely on additional conditional independence assumptions to facilitate support estimation. To solve for the support, the work [15] exploits a fast method such as graph cut, and the work [16] adopts a mean-field approximation. To avoid imposing such assumptions, a few attempts [13], [14], [17] solve the support estimation problem with heuristic [17] and the stochastic Markov Chain Monte Carlo approaches [13], [14]. Nevertheless, all these methods target structures obtained from training data. Thus, they are effective only to signals that are similar to those used in training, as they do not have the mechanism to adapt itself to effectively process signals with different structures. An example of an MRF obtained from training data is illustrated in Figure 2b. The trained MRF captures a universal pattern where all digits appear, whereas the adaptive MRF is much more tuned to a specific signal structure.

C. Cluster Structured Sparsity

Recent works [18]–[23] improve the group sparsity model by allowing the sparsity model parameters to adaptively update according to measurements. The goal is to handle unpredictable pattern of non-zero coefficients. These works often exploit two-state mixture models such as Gaussian-Gamma [21], [23] or beta-Bernoulli models [18]–[20] which are the canonical iid. models to model cluster structure. To enforce the clustered pattern, signal coefficients are grouped in clusters where they share the same set of the sparsity model parameters. The works [21], [23] capture the structure in the scale of sparse signals with Gaussian-Gamma model. Others [18]–[20] capture signal structure through supports where a multivariate Bernoulli distribution is used to model the structured sparsity. To achieve the same aim, the work [22] exploits the pairwise potentials of a Boltzmann machine distribution to model the cluster structure of sparse signals. Variational Bayesian expectation maximization methods are exploited to perform sparse signal recovery. Nevertheless, all these methods use fixed structures, and they require prior knowledge about the size and partition of the clusters that are often needed to be adjusted manually for different datasets.

In contrast to these methods, our adaptive MRF inference framework is based on the MRFs that can represent various types of sparse signals, and the underlying structure of the MRF can be automatically adjusted according to a specific signal structure.

III. GRAPHICAL COMPRESSIVE SENSING

In this study, we capture the structure of sparse signal \mathbf{x} by modelling its support explicitly. Let $\mathbf{s} \in \{-1, 1\}^N$ indicate the support of \mathbf{x} such that $s_i = 1$ when $x_i \neq 0$ and $s_i = -1$ when $x_i = 0$. Let $\mathbf{x}_s \in \mathbb{R}^k$ denote the non-zero coefficients of the k -sparse \mathbf{x} . Our goal is to estimate \mathbf{s} and \mathbf{x}_s from the linear measurements \mathbf{y} corrupted by additive noise \mathbf{n} as follows,

$$\mathbf{y} = \mathbf{A}_s \mathbf{x}_s + \mathbf{n}. \quad (1)$$

Here \mathbf{A}_s is the matrix with k columns selected from the matrix \mathbf{A} according to \mathbf{s} , and \mathbf{n} is the Gaussian white noise, *i.e.*, $\mathbf{n} \sim \mathcal{N}(\mathbf{0}, \sigma_n \mathbf{I})$ where σ_n is the noise variance and \mathbf{I} denotes an identity matrix with a proper size. The corresponding likelihood over \mathbf{y} can thus be formulated as

$$p(\mathbf{y} | \mathbf{x}_s, \mathbf{s}; \sigma_n) = \mathcal{N}(\mathbf{A}_s \mathbf{x}_s, \sigma_n \mathbf{I}). \quad (2)$$

Each observed measurement y_i can be seen a noisy linear combination of non-zero sparse signal coefficients that are projected on measurement matrix atoms. The interdependencies among coefficients can be modelled through the prior defined on \mathbf{s} . Specifically, we impose a graphical sparsity prior on \mathbf{x}_s and \mathbf{s} (Section III-A). Subsequently, we show how to recovery sparse signal \mathbf{x} from the measurements \mathbf{y} by our new adaptive MRF inference framework (Section III-B).

A. Graphical sparsity prior

The support \mathbf{s} often exhibits arbitrary and complex statistical dependency between its coefficients [17], [29]. MRFs are flexible and expressive enough to capture complex dependency by defining the probabilistic distribution of a undirected graph

structure [30], [31]. Specifically, by representing the considered variables as a graph $\mathcal{G} = (\mathcal{V}, \mathcal{E})$ where \mathcal{V} is a set of nodes (each representing a variable) and \mathcal{E} is a set of undirected edges. A set of parameterized potentials $\{\mathcal{W}_{(i,j)}(\cdot; \xi^{(i,j)})\}$ are defined in MRFs to represent the local dependency among all nodes. Moreover, MRFs are able to represent most geometric structures (*e.g.* block, tree, etc.) by updating the edges \mathcal{E} as well as the corresponding potentials, *viz.*, MRFs are capable of representing a wide range of signals with diverse structures [32]. To this end, we propose an MRF-based graphical sparsity prior to model the structure of sparse signal as follows.

First, we define the prior of support s based on MRFs. Let $\Theta_{\mathcal{G}}$ be a set of parameters of an MRF model with the structure defined by the underlying graph \mathcal{G} , *i.e.*, $\Theta_{\mathcal{G}} = \{\mathcal{W}_{(i,j)}(\cdot; \cdot), \xi^{(i,j)} | i \in \mathcal{V}, (i, j) \in \mathcal{E}\}$, and assume that each coefficient s_i in support s and each node $i \in \mathcal{V}$, have one-to-one mapping. Given the graph \mathcal{G} defined by node and edge sets $(\mathcal{V}, \mathcal{E})$, the probability of the support $p(s; \Theta_{\mathcal{G}})$ can be represented as follows with a normalization constant Z ,

$$\frac{1}{Z} \exp \left(\sum_{i \in \mathcal{V}} \mathcal{W}_i(s_i; \xi^i) + \sum_{(i,j) \in \mathcal{E}} \mathcal{W}_{i,j}(s_i, s_j; \xi^{(i,j)}) \right), \quad (3)$$

where $\mathcal{W}_{(i,j)}(\cdot; \xi^{(i,j)})$ is commonly assumed to be a linear function with respect to $\xi^{(i,j)}$; hence, the set of parameters is reduced to $\Theta_{\mathcal{G}} = \{\xi^{(i,j)}, \xi^{(i,j)} | i \in \mathcal{V}, (i, j) \in \mathcal{E}\}$. The first term of Eq.(3) defines bias (*e.g.*, confidence) potential to each s_i ; while the second term characterizes interaction between them, *i.e.*, $\xi^{(i,j)}$ weights the dependency between s_i and s_j .

In addition, we assume x comes from a Gaussian distribution $\mathcal{N}(0, \Sigma_x)$ where Σ_x is a diagonal matrix. Given s , the probability of non-zero coefficients $p(x_s | s) = \mathcal{N}(0, \Sigma_{x,s})$ where $\Sigma_{x,s}$ is a diagonal matrix whose diagonal entry is chosen from Σ_x according to s . Then, $p(x_s | s)p(s; \Theta_{\mathcal{G}})$ forms the graphical sparsity prior in this study.

B. Adaptive Markov Random Fields inference

Provided that these optimum parameters $\hat{\sigma}_n$, $\hat{\Sigma}_{x,s}$, $\hat{\Theta}$, and $\hat{\mathcal{G}}$ are given beforehand, the latent x_s and s can be estimated by solving a maximum a posteriori (MAP) problem as

$$\max_{x_s, s} p(x_s, s | y) \propto p(y | x_s, s; \hat{\sigma}_n) p(x_s | s; \hat{\Sigma}_{x,s}) p(s; \hat{\Theta}_{\mathcal{G}}). \quad (4)$$

However, these parameters are often unknown in real applications. Some previous works obtain both of the MRF's parameters and underlying graph from training data [14], [16], [17]. While the resulting prior parameters can well fit the common characteristics among training data, they fail to adapt to testing data.

In this study, we propose the adaptive MRF inference framework where all the parameters—the MRF's model parameters and its corresponding graph $\Theta_{\mathcal{G}}$ and \mathcal{G} , and noise and signal parameters σ_n and $\Sigma_{x,s}$ —are adaptively updated according to measurements. To enable adaptive MRF inference framework without incurring high computation, our method will estimate σ_n , $\Sigma_{x,s}$, and $\Theta_{\mathcal{G}}$ from the measurements y . Meanwhile, the underlying graph \mathcal{G} is updated according to non-zero coefficients in an estimated support. The process of updating the graph \mathcal{G} are described in Section III-B2.

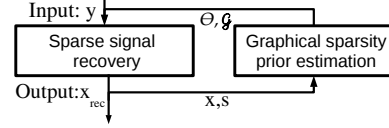


Fig. 3: Visualization of our Adaptive MRF inference framework

Our objective is to estimate these parameters— σ_n , $\Sigma_{x,s}$, and $\Theta_{\mathcal{G}}$ —from the measurements by solving

$$\max_{s, \sigma_n, \Sigma_{x,s}, \Theta_{\mathcal{G}}} p(y | s, \sigma_n, \Sigma_{x,s}, \Theta_{\mathcal{G}}) \propto \int p(y | x_s, \hat{s}, \sigma_n) p(x_s | \hat{s}, \Sigma_{x,s}) p(\hat{s} | \Theta_{\mathcal{G}}) dx_s, \quad (5)$$

which intrinsically maximizes the likelihood of measurements over all model parameters as well as the support. Solving Eq. (5) directly is intractable. To circumvent this problem, we reduce Eq. (5) into two subproblems as follows.

1) Sparse signal recovery

Given $\hat{\Theta}_{\mathcal{G}}$ and $\hat{\mathcal{G}}$, we first infer other parameters from the measurements by solving

$$\max_{s, \sigma_n, \Sigma_{x,s}} p(y | s, \sigma_n, \Sigma_{x,s}) \propto \int p(y | x_s, s, \sigma_n) p(x_s | s, \Sigma_{x,s}) p(s | \hat{\Theta}_{\mathcal{G}}) dx_s. \quad (6)$$

With the given $\hat{\Theta}_{\mathcal{G}}$, $\hat{\mathcal{G}}$, and the estimated \hat{s} , $\hat{\sigma}_n$, and $\hat{\Sigma}_{x,s}$, the sparse signal x_s can be then estimated as Eq. (4). These two steps are integrated into a unified variational framework in Section III-C, which can be optimized effectively.

2) Graphical sparsity prior estimation

Given the estimated \hat{x}_s , \hat{s} , $\hat{\sigma}_n$, and $\hat{\Sigma}_{x,s}$, we have

$$\begin{aligned} p(y | \Theta_{\mathcal{G}}) &= \int p(y | x_s, s, \hat{\sigma}_n) p(x_s | s, \hat{\Sigma}_{x,s}) p_{\mathcal{G}}(s | \Theta_{\mathcal{G}}) dx_s \\ &\approx p(y | \hat{x}_s, \hat{s}, \hat{\sigma}_n) p(\hat{x}_s | \hat{s}, \hat{\Sigma}_{x,s}) p(\hat{s} | \Theta_{\mathcal{G}}), \end{aligned} \quad (7)$$

where the likelihood is approximated by the pointwise maximum within the integral term. Let $\hat{\mathcal{G}}$ be given, the parameter $\Theta_{\mathcal{G}}$ therefore can be inferred as

$$\max_{\Theta_{\mathcal{G}}} p(\hat{s}, \Theta_{\mathcal{G}}) = p(\hat{s} | \Theta_{\mathcal{G}}) p(\Theta_{\mathcal{G}}), \quad (8)$$

which encourages $\Theta_{\mathcal{G}}$ (*i.e.*, graphical sparsity prior) to be adaptive to the distribution of the latent support signal. In practice, we use $p(\Theta_{\mathcal{G}})$ as a uniform distribution.

The graph \mathcal{G} can be estimated from structure learning approaches such as score-based learning which, however, will require running inference on each of the candidate graph structures [30].

Update Graph \mathcal{G} : In practice, we can simplify the graph estimation task, as suggested by [11], by forming a graph according to k non-zero coefficients in the estimated support \hat{s} which carry information about signal structure. The graph update procedure is provided in Algorithm 1 where each coefficient is mapped to each node, and only non-zero nodes form edges to its adjacent nodes. Algorithm 1 can be extended to capture the signal structure in two-dimensional images by mapping each pixel to a node in the graph, and each edge

Algorithm 1: Update Graph \mathcal{G} **Input :** Support vector \mathbf{s}

- 1) Establish each node corresponds to each coefficient in a support vector;
- 2) For every node corresponding to a non-zero coefficient, establish edges from the non-zero node i to its adjacent nodes in its neighbourhood \mathbb{N}_i ;
- 3) Remove redundant edges, *i.e.*, remove the edge $j - i$, if the edge $i - j$ is established (where $j > i$).

Output: $\mathcal{G} = (\mathcal{V}, \mathcal{E})$.

connects a non-zero node i to its adjacent node in a neighbour set \mathbb{N}_i .

Remark: The sparseness of the graph depends on the non-zero coefficients in the estimated support $\hat{\mathbf{k}}$ and the size of the neighbour set \mathbb{N}_i . The sparseness can help accelerate graphical model inference process (see Section III-D). For example, for 1D support with the \hat{k} sparsity, if the set of neighbours is defined as $\mathbb{N}_i = \{i - 1, i + 1\}$, the graph becomes a chain graph which contains $2\hat{k}$ edges. For this special case, the graphical model inference problem can be solved exactly with a belief propagation with $\mathcal{O}(\hat{k})$ complexity.

The two subproblems Eq. (6) and Eq. (8) are then alternatively optimized until they converge. Figure 3 illustrates the proposed adaptive MRF inference framework. The estimated sparse signal is able to refine the graphical sparsity prior, while the refined graphical sparsity prior results in a more accurate sparse recovery. After these two processes iterate until they converge, we obtain the final result.

C. Optimization.

Since the graphical sparsity prior estimation in Eq. (8) can be effectively solved by many off-the-shelf MAP inference solvers [30], [32], [33]. Here, we mainly focus on solving the optimization Eq. (6), given the graphical sparsity prior, *i.e.*, MRF parameters $\hat{\Theta}_{\hat{\mathcal{G}}}$ and the underlying graph $\hat{\mathcal{G}}$. The optimization problem in Eq. (6) can be equally reformulated as [17], [34]

$$\min_{\mathbf{s}, \sigma_n, \Sigma_{x,s}} -\log \int p(\mathbf{y}|\mathbf{x}_s, \mathbf{s}, \sigma_n) p(\mathbf{x}_s|\mathbf{s}, \Sigma_{x,s}) p(\mathbf{s}; \hat{\Theta}_{\hat{\mathcal{G}}}) d\mathbf{x}_s \equiv \frac{1}{2} \mathbf{y}^T (\sigma_n \mathbf{I} + \mathbf{A}_s \Sigma_{x,s} \mathbf{A}_s^T)^{-1} \mathbf{y} + \frac{1}{2} \log |\sigma_n \mathbf{I} + \mathbf{A}_s \Sigma_{x,s} \mathbf{A}_s^T| - \log p(\mathbf{s}|\hat{\Theta}_{\hat{\mathcal{G}}}). \quad (9)$$

Even fixing \mathbf{s} , the remaining problem of Eq. (9) is still non-convex, and there are no closed-form solutions for σ_n and $\Sigma_{x,s}$. And after solving Eq. (9), one still has to estimate \mathbf{x} .

We propose to use a strict upper bound of Eq. (9) in the spirit of [24], [25]. This allows us to have closed-form solutions for σ_n and $\Sigma_{x,s}$. Moreover, \mathbf{x} , σ_n , and $\Sigma_{x,s}$ are jointly estimated in a single framework instead of the two-step approach in Eq. (9) :

$$\mathbf{y}^T (\sigma_n \mathbf{I} + \mathbf{A}_s \Sigma_{x,s} \mathbf{A}_s^T)^{-1} \mathbf{y} = \inf_{\mathbf{x}} \frac{1}{\sigma_n} (\mathbf{y} - \mathbf{A}_s \mathbf{x}_s)^T (\mathbf{y} - \mathbf{A}_s \mathbf{x}_s) + \mathbf{x}_s^T \Sigma_{x,s}^{-1} \mathbf{x}_s. \quad (10)$$

With this bound, the cost function Eq. (9) can be transformed into a new cost function as

$$L(\mathbf{x}_s, \mathbf{s}, \sigma_n, \Sigma_{x,s}) = \frac{1}{2\sigma_n} (\mathbf{y} - \mathbf{A}_s \mathbf{x}_s)^T (\mathbf{y} - \mathbf{A}_s \mathbf{x}_s) + \frac{1}{2} \mathbf{x}_s^T \Sigma_{x,s}^{-1} \mathbf{x}_s + \frac{1}{2} \log |\sigma_n \mathbf{I} + \mathbf{A}_s \Sigma_{x,s} \mathbf{A}_s^T| - \log p(\mathbf{s}; \hat{\Theta}_{\hat{\mathcal{G}}}). \quad (11)$$

Thus, the sparse signal \mathbf{x}_s , the support \mathbf{s} , and other model parameters σ_n and $\Sigma_{x,s}$ are jointly optimized. Moreover, it can be proved that the resulting \mathbf{s} , σ_n , $\Sigma_{x,s}$ from minimizing the new cost function Eq. (11) are equivalent to that from solving Eq. (9) [24], [25]. Therefore, we turn to optimize Eq. (11) to obtain all involved unknown variables as:

$$\{\hat{\mathbf{x}}, \hat{\mathbf{s}}, \hat{\sigma}_n, \hat{\Sigma}_{x,s}\} = \min_{\mathbf{x}_s, \mathbf{s}, \sigma_n, \Sigma_{x,s}} L(\mathbf{x}_s, \mathbf{s}, \sigma_n, \Sigma_{x,s}). \quad (12)$$

Since Eq. (12) involves several unknown variables, we adopt an alternative minimization scheme to reduce the original problem into several subproblems each of which only involves one variable and often can be solved directly. These subproblems are then optimized alternatively until convergence. We only provide the solution of each sub-problem as follows. The detail derivation is provided in Appendix.

1) Optimization over \mathbf{s}

Given \mathbf{x} , σ_n , and $\Sigma_{x,s}$, the subproblem over the support \mathbf{s} can be given as

$$\min_{\mathbf{s}} \frac{1}{2\sigma_n} \mathbf{x}_s^T \mathbf{A}_s^T \mathbf{A}_s \mathbf{x}_s - \frac{1}{\sigma_n} \mathbf{y}^T \mathbf{A}_s \mathbf{x}_s + \frac{1}{2} \mathbf{x}_s^T \Sigma_{x,s}^{-1} \mathbf{x}_s + \frac{1}{2} \log |\sigma_n \mathbf{I} + \mathbf{A}_s \Sigma_{x,s} \mathbf{A}_s^T| - \log p(\mathbf{s}; \hat{\Theta}_{\hat{\mathcal{G}}}). \quad (13)$$

According to the Hadamard product properties, the objective function in Eq. (13) can be equally reformulated as

$$\min_{\mathbf{v} \in \{0,1\}^N} \frac{1}{2\sigma_n} \mathbf{v}^T (\mathbf{X}^T \mathbf{A}^T \mathbf{A} \mathbf{X} + \sigma_n \mathbf{X}^T \Sigma_x^{-1} \mathbf{X}) \mathbf{v} + (-\frac{1}{\sigma_n} \mathbf{y}^T \mathbf{A} \mathbf{X} + \mathbf{p}^T + \mathbf{q}^T) \mathbf{v} - \log p(2\mathbf{v} - 1; \hat{\Theta}_{\hat{\mathcal{G}}}), \quad (14)$$

where $\mathbf{v} = \frac{1}{2}(\mathbf{s} + 1)$, $\mathbf{p} = \frac{1}{2} \log(\text{diag}\{\Sigma_x\})$, $\mathbf{q} = \frac{1}{2} \log(\text{diag}\{\sigma_n \Sigma_x^{-1} + \mathbf{V}'^T \mathbf{A}^T \mathbf{A} \mathbf{V}'\})$, and \mathbf{X} is a diagonal matrix with diagonal coefficients from \mathbf{x} . \mathbf{V}' is a diagonal matrix with diagonal coefficients from \mathbf{v}' where $\mathbf{v}' = \frac{1}{2}(\mathbf{s}' + 1)$ and \mathbf{s}' is the support from previous iteration.

The minimization problem in Eq. (14) can be viewed as an MAP problem over an MRF model. The first two terms can be viewed as the pairwise and unary terms, respectively. Meanwhile, $p_{\hat{\mathcal{G}}}(2\mathbf{v} - 1; \hat{\Theta}_{\hat{\mathcal{G}}})$ in the third term is a typical MRF model (see Section III-A). Eq. (14) can be effectively solved by any off-the-shelf inference tools, *e.g.*, Dual Decomposition [35], TWRS [36], ADLP [37]. However, the inference process can slow down especially when the coefficients of the estimated sparse signals \mathbf{x} are all non-zero, *i.e.*, the first term $(\mathbf{X}^T \mathbf{A}^T \mathbf{A} \mathbf{X} + \sigma_n \mathbf{X}^T \Sigma_x^{-1} \mathbf{X})$ becomes a pairwise potential matrix representing a fully connected graph.

Accelerating support estimation: To keep processing time low, we exploit the fact that in compressive sensing system, the measurement matrix \mathbf{A} usually satisfies the restricted isometric

property [38], *i.e.*,

$$\|A_s^* A_s - I\|_{2 \rightarrow 2} \leq \delta_s, \quad (15)$$

where I is an identity matrix, $\|\cdot\|_{2 \rightarrow 2}$ is the operator norm, and δ_s is the corresponding restricted isometric constant. Hence, the first term in Eq. (14) can be approximated as follows

$$v^T (X^T A^T A X + \sigma_n X^T \Sigma_x^{-1} X) v \approx v^T X^T (Q + \sigma_n \Sigma_x^{-1}) X v \quad (16)$$

where Q is a diagonal matrix whose diagonal entries are the diagonal entries of $A^T A$. Thus, we solve for the signal support by solving the following optimization problem:

$$\min_{v \in \{0,1\}^N} \left(\frac{1}{2\sigma_n} r^T - \frac{1}{\sigma_n} y^T A X + p^T + q^T \right) v - \log p(2v - 1; \hat{\Theta}_{\hat{G}}), \quad (17)$$

where r is a vector containing diagonal entry of the matrix $(X^T (Q + \sigma_n \Sigma_x^{-1}) X)$. The pairwise term in Eq.(16) reduces to a unary term which is much faster to evaluate. The computational complexity for solving Eq.(17) depends only on the underlying graph of the updated MRF defined by $\hat{\Theta}_{\hat{G}}$ (see Section III-D).

2) Optimization over σ_n

Given x_s , s and $\Sigma_{x,s}$, we have the sub-problem over σ_n

$$\min_{\sigma_n} \frac{1}{2\sigma_n} (y - A_s x_s)^T (y - A_s x_s) + \frac{1}{2} \log |\sigma_n I + A_s \Sigma_{x,s} A_s^T|. \quad (18)$$

This problem gives rise to a closed-form solution for σ_n as

$$\sigma_n^{new} = \frac{1}{M} \sum_{i=1}^M \sqrt{\frac{d_i^2}{\eta_i}}. \quad (19)$$

where η_i is the i -th entry of vector $\eta = \text{diag}\{(\sigma_n I + A_s \Sigma_{x,s} A_s^T)^{-1}\}$, and d_i is the i -th entry of $d = y - A_s x_s$.

3) Optimization over $\Sigma_{x,s}$

We start from calculating Σ_x , then $\Sigma_{x,s}$ is chosen from the diagonal member of Σ_x according to s . Let $\nu \in \mathbb{R}_+^N$ be a vector whose members are the diagonal entry of Σ_x . Given x , s , and σ_n , we have the sub-problem over Σ_x as

$$\min_{\nu} \frac{1}{2} x^T \Sigma_x^{-1} x + \frac{1}{2} \log |\sigma_n I + A V \Sigma_x V^T A^T|, \quad (20)$$

where V is a diagonal matrix with diagonal coefficients from $v = \frac{1}{2}(s + 1)$. The updated equation for the i -th entry of ν is

$$\nu_i^{new} = x_i^2 + \alpha_i. \quad (21)$$

α_i is the i -th entry of vector $\alpha = \text{diag}\{(\Sigma'_x + \frac{1}{\sigma_n} V^T A^T A V)^{-1}\}$, and Σ'_x is the resulted Σ_x in previous iteration. Then, $\Sigma_{x,s}$ is diagonal matrix where each diagonal coefficient ν_i^{new} are chosen according to s .

4) Optimization over x_s

Given s , σ_n , and $\Sigma_{x,s}$, the subproblem for x_s is

$$\min_{x_s} \frac{1}{\sigma_n} (y - A_s x_s)^T (y - A_s x_s) + x_s^T \Sigma_{x,s}^{-1} x_s, \quad (22)$$

which shows a closed-form updated equation as

$$x_s^{new} = (\sigma_n \Sigma_{x,s}^{-1} + A_s^T A_s)^{-1} A_s^T y. \quad (23)$$

Algorithm 2: Sparse signal recovery.

Input : A measurement signal y , A , and graphical model's parameters Θ_G and structure G

Initialization: $\Sigma_x = I_{N \times N}$, $\sigma_n = 1$, and $x = 0$;

while a stopping criterion is not satisfied **do**

1. Update the support s by solving Eq. (17) ;
2. Update the noise variance σ_n as Eq. (19) ;
3. Update the covariance matrix $\Sigma_{x,s}$ as Eq. (21) ;
4. Update the sparse signal x_s as Eq. (23) ;

end

Output : x whose non-zero coefficients are from x_s

Algorithm 3: Adaptive Markov Random Field inference for compressive sensing (Adaptive-MRF)

Input : Measurements y and random matrix A

Initialization : Get x from Algorithm 2 where step 1 is removed and replaced with a fixed $s = 1$;

while a stopping criterion is not satisfied **do**

1. Obtain s from thresholding each of x , *i.e.*, $s_i = 1$ if $\text{abs}(x_i) > \text{mean}(\text{abs}(x))$, and $s_i = -1$ otherwise ;
2. Calculate G from s following Algorithm 1 ;
3. Estimate Θ_G from s and G by solving Eq. (8) ;
4. Update x by solving Eq.(12) with Algorithm 2;

end

Output : Recovered x_{rec} .

How to solve Eq. (12) is summarized in Algorithm 2 where sparse signal recovery, support estimation, and noise and signal parameters estimation are integrated in a unified framework. Given Algorithm 2, the whole adaptive MRF inference framework is summarized in Algorithm 3. The alternative minimization scheme reduces the objective function in each iteration, and the objective function can be proved to be bounded from below. Thus, the two algorithms converge well as [24]. To confirm this, we also provide empirical convergence of Adaptive-MRF in Section IV-F.

Here, we turn to the MRF parameters estimation problem Eq.(8) in step 3 in Algorithm 3. The MRF parameter estimation problem is solved by the pseudo-likelihood learning algorithm provided by [33]. The underlying graph in step 2 are estimated based on the support obtained from step 1 that truncates negligible sparse signal coefficients in x to zero. Thus, the MRF captures the structure of high energy coefficients in x . In Algorithm 2, we solve the support estimation problem Eq. (14) in step 1 by performing graphical inference using the belief propagation implemented in [39].

D. Algorithm Complexity

Dominant computation of the proposed method involves the computation in support estimation Eq. (17), and the matrix inversion for α in Eq. (21), η in Eq. (19) and x_s in Eq. (23) in the proposed signal recovery (Algorithm 2). The computational complexity of the proposed signal recovery is $\mathcal{O}(t_{max} \hat{k} |N| + 2M^3)$, which is reduced from $\mathcal{O}(t_{max} |\mathcal{E}| + N^3 + M^3 + \hat{k}^3)$ where \hat{k} is the sparsity of the estimated support. Note that \hat{k} can be any value from 0 to N depending on the he estimated support from step 1 Algorithm 2. $|\mathcal{E}|$ is maximum number of edges

in the underlying graph \mathcal{G} , and t_{max} denotes the maximum number of iteration in performing the belief propagation. The computational complexity depends on not only the dimension of signals but also the structure of the graph \mathcal{G} , and it can be kept low using matrix inversion properties, which are discussed as follows:

The complexity of support estimation Eq. (17) using the belief propagation algorithm based on MAP LP-relaxations [39] is $\mathcal{O}(t_{max}|\mathcal{E}|)$ which depends on the graph \mathcal{G} that is obtained from Algorithm 1 in Section III-B2. The graph \mathcal{G} models correlation between non-zero coefficients and their neighbours in the small regions. Thus, $|\mathcal{E}| = \hat{k}|\mathbb{N}|$ and \mathbb{N} is the largest set of neighbouring nodes. If \mathbb{N} covers only two adjacent nodes such as in a chain graph, $|\mathbb{N}|$ can be very small. For this special case, $\mathcal{O}(t_{max}\hat{k}|\mathbb{N}|) \approx \mathcal{O}(t_{max}\hat{k})$.

The matrix inversion in Eq. (21), in Eq. (19), and in Eq. (23) costs $\mathcal{O}(N^3 + M^3 + \hat{k}^3)$ which can be reduced to $\mathcal{O}(2M^3)$ by employing matrix inversion properties. Let us first consider the matrix inversion in Eq. (21). We can use the following matrix inversion property to reduce the cost of $\mathcal{O}(N^3)$ to $\mathcal{O}(M^3)$:

$$\begin{aligned} (\Sigma_x'^{-1} + \frac{1}{\sigma_n} \mathbf{V}^T \mathbf{A}^T \mathbf{A} \mathbf{V})^{-1} &= \Sigma_x' - \\ \Sigma_x' \mathbf{V}^T \mathbf{A}^T (\sigma_n \mathbf{I} + \mathbf{A} \mathbf{V} \Sigma_x' \mathbf{V}^T \mathbf{A}^T)^{-1} \mathbf{A} \mathbf{V} \Sigma_x', \end{aligned} \quad (24)$$

where the matrix inversion requires $\mathcal{O}(M^3)$ and $M \ll N$. One can employ a similar technique to reduce the computation for matrix inversion in Eq. (23) and Eq. (19) to $\mathcal{O}(M^3)$. Therefore, the total computational complexity of Algorithm 2 is reduced to $\mathcal{O}(t_{max}\hat{k}|\mathbb{N}| + 2M^3)$ in each iteration. If the underlying graph \mathcal{G} is a chain graph, the computational cost can be reduced to $\mathcal{O}(t_{max}\hat{k} + 2M^3)$ which is $\approx \mathcal{O}(2M^3)$. This can be seen as close to $\mathcal{O}(M^3)$ of [25] that also exploits a similar latent variable Bayes model [24]; nevertheless, [25] does not consider the correlation between signal coefficients.

The computation of Algorithm 2 is included in step 4 of Algorithm 3 (our Adaptive-MRF). The runtime performance of our Adaptive-MRF is provided in Figure 14 and 15 (see Section IV-H3). We can see that the runtime of our method is moderate among all methods.

IV. EXPERIMENTAL RESULTS AND ANALYSIS

In this section, we study the performance of the proposed Adaptive-MRF on recovering sparse signals with different structures. We test the performance on three datasets—MNIST [40], CMU-1DB [41], and CIFAR-10 [42]—which exhibit different characteristics, detailed in Section IV-A. The comparison methods, evaluation criterion, and experiment setting are given in Section IV-B, IV-C, and IV-D. Section IV-E illustrates the effectiveness of Adaptive-MRF in comparison with signal recovery with a trained MRF that is fixed through out the signal recovery process (Fixed-MRF). The convergence of Adaptive-MRF is provided in Section IV-F. Then, we study the performance of our proposed sparse signal recovery in comparison with the method [17] and [14] in adaptive MRF framework in Section IV-G. The performance of the proposed Adaptive-MRF is then compared with state-of-the-art competitors in terms of compressibility, noise tolerance, and runtime in Section IV-H.

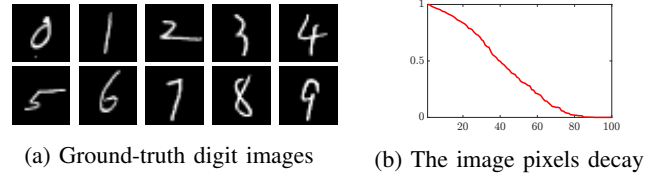


Fig. 4: MNIST. (a) The ground truth handwritten digit images. (b) The pixel coefficient's decay.

A. Dataset

We evaluate the performance on three datasets—MNIST [40], CMU-1DB [41], and CIFAR-10 [42]—which exhibit different characteristics: i) *MNIST handwritten digit images* [40] contain few long-continued lines and are strictly sparse. ii) *CMU-1DB face image dataset* [41] contains similar facial features which have dense spatial information. This is opposite to MNIST dataset. iii) *CIFAR-10 natural images dataset* [42] are more diverse and less synthesized than the previous two datasets. They reflect the performance on typical images. The images selected for the experiment from each dataset are shown in Figure 4a, 5a, 6a.

The MNIST digit images are strictly sparse, as shown in the pixel decay curve Figure 4b. The compression process can be applied onto the signals directly. However, images from CMU-1DB and CIFAR-10 datasets are not sparse. Their sparse representation can be obtained by transforming these images into an appropriate basis. Here, we exploit i) wavelet transform, ii) discrete cosine transform (DCT), and iii) principal component analysis (PCA) to obtain these sparse representation. Examples of the sparse representation in wavelet, DCT, and PCA domains of CMU-1DB and CIFAR-10 images are in Figure 5b, 5c, 5d and Figure 6b, 6c, 6d, respectively. It can be seen that the signal representation of CMU-1DB images are equally sparse in PCA and DCT domain; meanwhile, the signal representations of natural images from CIFAR-10 are sparse in DCT and Wavelet. Note that the signal representations of CIFAR-10 images in PCA domain is very dense; thus, it violates the sparsity assumption of compressive sensing.

Hence, we mainly focus on the experimental results and analysis on the MNIST digit images, the PCA signals from CMU-1DB, and the wavelet signals from CIFAR-10 datasets in this paper. The experimental results for DCT and Wavelet signals of CMU-1DB and DCT signals of CMU-1DB CIFAR-10 datasets are provided in *Section I in the supplementary material*.

B. Comparison methods

The performance of our method is compared with 10 state-of-the-art competitors:

- **Existing MRF-based methods:** MAP-OMP¹ [17], Gibbs¹ [14] —whose support estimation are based on solving the optimization problem Eq.(9) with heuristic and stochastic approaches — and LAMP [15] and SSoBaP¹ [16]—that imposes additional conditional independence assumptions;

¹The graphical model, noise and signal variance parameters provided to MAP-OMP, Gibbs, and SSoBaP is from training data.

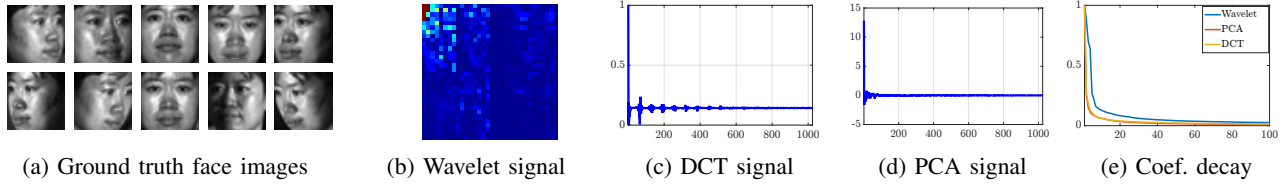


Fig. 5: CMU-IBD. (a) The ground truth face images. Examples of (b) wavelet signal, (c) DCT signal, (d) PCA signal, and (e) the decay of sparse signal coefficients in wavelet, DCT, and PCA domain.

- **Clustering structured sparsity-based methods:** MBCS-LBP² [20] and Pairwise MRF² [22];
- **Graph sparsity-based methods:** GCoSamp [11] and StructOMP [4]
- **Sparsity-based methods:** a Bayesian-based method RLPHCS [25] and a standard signal recovery method OMP [34].
- We use *the oracle estimator* suggested in [17] that uses **the ground truth support** to estimate the signal (via Eq. (23)). Note that all other methods do not have the access to the ground truth support. The oracle estimator has this unfair advantage, and we use it to show the best possible result using ground truth support with homogeneous noise parameters.

All of the comparison methods, except Pairwise MRF [22], are implemented by the code of the authors with tuned parameters to the best performance. For Pairwise MRF, we implemented the code ourselves. Here, 8-neighbouring system is used to calculate the local cluster structure, and we set the Pairwise MRF algorithm to terminate when the minimum update difference is less than 10^{-3} , or when the iteration reaches 200.

C. Evaluation criterion

We demonstrate the proposed Adaptive-MRF performance on recovery accuracy, noise tolerance, and runtime performance. The recovery accuracy is evaluated by peak signal to noise ratio (PSNR). We show the runtime curves versus sampling rate (M/N) and the runtime curves versus the sparsity levels (k) which is defined as the number of non-zero coefficients in a sparse signal. Since the signal representations of CMU-IBD and CIFAR-10 images are not strictly sparse, we use an approximate sparsity level (\tilde{k}) defined as the number of high-energy coefficients that contributes 99% of signal energy.

Empirical convergence of Adaptive-MRF is analyzed through observing the decay of the cost function value Eq.(11) and the minimum update difference value which is also used for terminating the proposed algorithm. The minimum update difference between the two consecutive estimates of \mathbf{x} is defined as

$$\eta = \frac{\|\mathbf{x}^{new} - \mathbf{x}\|_2}{\|\mathbf{x}\|_2}. \quad (25)$$

This is to ensure that our algorithm provides the result that converges to a desired solution, along with the decay of both value.

D. Experimental settings

In the compression, the sparse signal \mathbf{x} is sampled by a random Bernoulli matrix \mathbf{A} to generate the linear measurements \mathbf{y} . The recovery performance is tested across different sampling rates (M/N), i.e., 0.2, 0.25, 0.3, 0.35, and 0.4. To simulate the noise corruption on measurements, 4 different levels of Gaussian white noise are added into \mathbf{y} , which results in the signal to noise ratio (SNR) to be 5 dB, 10 dB, 20 dB, and 30 dB³.

Algorithm Setting: The proposed Adaptive-MRF (Algorithm 3: the main algorithm) will stop when the minimum update difference of \mathbf{x} from step 4 is less than 10^{-3} , or when the maximum iteration is reached. Here, the maximum iteration is set to 3. In step 2, the graph update is performed where the set of neighbours of the non-zero node i , namely \mathbb{N}_i , covers its 8 neighboring nodes. In step 3, the MRF parameters are estimated using the package [33] where the maximum iteration is set to 20. In step 4, the sparse signal recovery is performed by Algorithm 2 which is set to terminate when the minimum update difference of \mathbf{x}_s is less than 10^{-3} , or when the iteration reaches 200.

E. Effectiveness of Adaptive-MRF.

To reflect the improved performance due to adaptive MRF inference framework, we compare the performance of the proposed Adaptive-MRF against the performance when an MRF is fixed. By that an MRF is fixed, we mean the sparse signal recovery (Algorithm 2) exploits a trained MRF which is fixed through out the signal recovery process and where both the underlying graph and parameters are obtained from training; thus, it is denoted as *Fixed-MRF*. Figure 7 shows the bar graph of the average PSNR value across different sampling rates on the three datasets—MNIST handwritten images, PCA sparse signals of CMU-IBD face images, and wavelet sparse signals of CIFAR-10 natural images— at noise level (SNR) of 30 dB. It is clear that Adaptive-MRF outperforms Fixed-MRF in all cases, especially when sampling rate (M/N) is higher than 0.2, Adaptive-MRF outperforms Fixed-MRF by at least 2 dB on MNIST images, 2 dB on CMU-IBD images, and 0.5 dB on CIFAR-10 images.

F. Convergence of Adaptive-MRF.

In this section, we study empirical convergence of Adaptive-MRF by observing the decay of the cost function value Eq.(11) and the minimum update difference value (η) Eq.(25). To study the convergence of Adaptive-MRF, we set the maximum iteration of the adaptive MRF inference framework to 5, and

²For both MBCS-LBP and Pairwise MRF, we use 8-neighbour system to capture local cluster structure

³The noise level (in SNR) from 5 dB to 30 dB is the highest to the lowest noise corruption

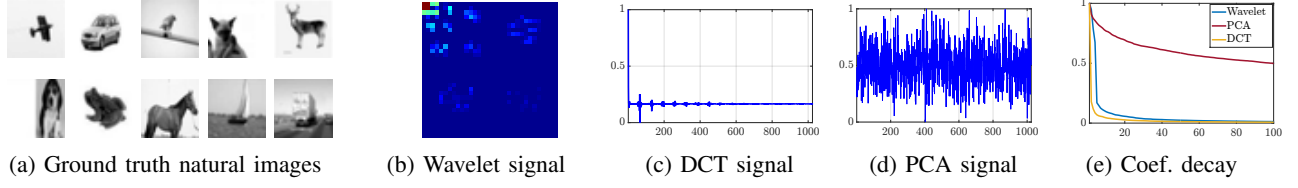


Fig. 6: CIFAR-10. (a) The ground truth natural images. Examples of (b) wavelet signal, (c) DCT signal, (d) PCA signal, and (e) the decay of sparse signal coefficients in wavelet, DCT, and PCA domain.

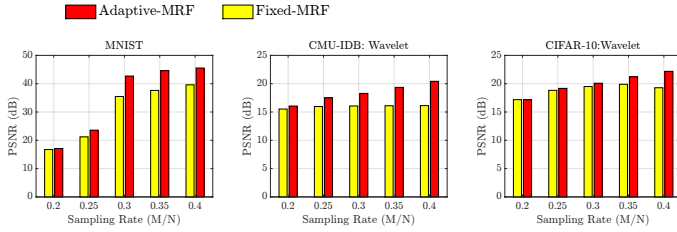


Fig. 7: Comparison of the Adaptive-MRF and Fixed-MRF on MNIST dataset, CMU-1DB dataset, and CIFAR-10 dataset under noise level (SNR) of 30 dB.

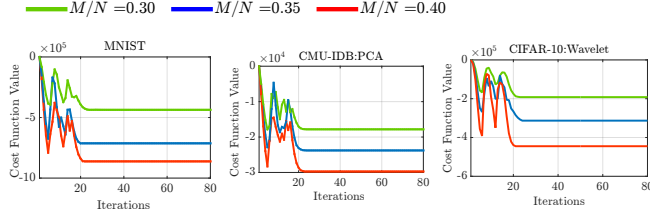


Fig. 8: Convergence of the cost function value of the Adaptive-MRF on three datasets under sampling rate of 0.3 and noise level (SNR) of 30 dB.

we set the process of sparse signal recovery running in the loop to terminate when minimum update difference of the signal is less than 10^{-3} , or when the iteration reaches 200.

Figure 8 and Figure 9⁴ provide convergence of Adaptive-MRF on the three datasets in terms of the cost function value, and the minimum update difference when noise level (SNR) is set to 30 dB. The *iterations* on the horizontal axis of each graph denotes the total iterations where the signal recovery process is performed at the inner-loop, and the adaptive MRF inference framework is performed at the outer-loop. In most cases, Adaptive-MRF converges after running the outer-loop for 3 times, which can be observed from ripples appear in the cost function value curves. The duration of performing the signal recovery process in each loop is about 7 iterations which further minimizes the cost function value until the minimum update difference is less than 10^{-3} . This suggests that the estimated MRF helps improve sparse signal recovery, and vice versa. The total number of iterations that Adaptive-MRF takes to converge is less than 30 iterations. Therefore, our Adaptive-MRF converges after few iterations.

⁴Here, we add a value of 0.05 and 0.1 to the minimum update difference curves when $M/N = 0.35$ and 0.4 , respectively, to provide the clear visibility of the two curves.

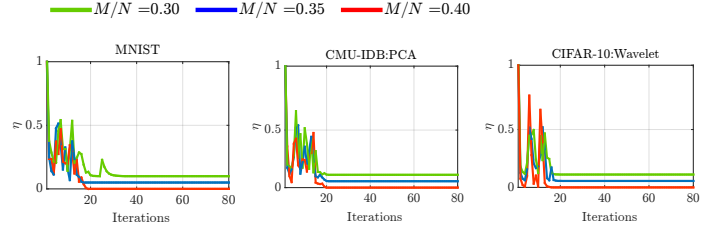


Fig. 9: Convergence of the minimum update difference (η) of the Adaptive-MRF on three datasets under sampling rate of 0.3 and noise level (SNR) of 30 dB.

G. Effectiveness of the proposed sparse signal recovery.

In this section, we demonstrate the effectiveness of our sparse signal recovery that obtains the sparse signal from solving the new optimization problem Eq. (11) whose cost function is the upper bound approximation of Eq. (9). Here, we compare the performance of our sparse signal recovery against Gibbs [14] and MAP-OMP [17] that attempt to solve Eq. (9) directly with the stochastic and heuristic approaches. All the algorithms are tested in the same adaptive MRF inference framework setting. Thus, we compare our Adaptive-MRF against Adaptive-Gibbs (Gibbs + the adaptive MRF inference framework) and Adaptive-MAP-OMP (MAP-OMP + the adaptive MRF inference framework). The adaptive MRF inference framework performing as the main-loop is set to terminate when the number of iteration reach to 3. The sparse recovery process performs at the inner-loop. All the sparse recovery algorithms are set to terminate when the iteration reaches 1000, or when minimum update differences between two consecutive estimate \mathbf{x} is less than 10^{-5} .

Figure 10 illustrates the recovery performance across six datasets (no. 1-6): no. (1) denotes MNIST handwritten images; no. (2)(3)(4) denote sparse representation of CMU-1DB face images in wavelet, DCT, and PCA domain; and no. (5)(6) denote sparse representation of CIFAR-10 natural images in wavelet and DCT domains. The performance is tested at the sampling rate and noise level (SNR) of 0.3 and 30 dB, respectively. It is clear that Adaptive-MRF requires the least runtime and provides the highest accuracy in all cases.

To further examine the performance of the proposed Adaptive-MRF in terms of speed, Figure 11a and 11b illustrate the convergence of average accuracy and runtime per iteration of our Adaptive-MRF against Adaptive-Gibbs and Adaptive-

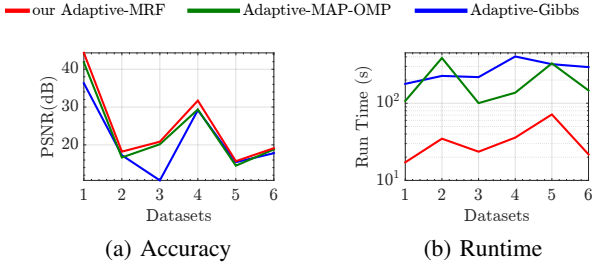


Fig. 10: Solving Eq. (11) (our Adaptive-MRF) vs solving Eq. (9) directly (Adaptive-Gibbs and Adaptive-MAP-OMP) in terms of (a) recovery accuracy and (b) total runtime on 6 datasets. The sampling rate is 0.3 and noise level (SNR) is 30 dB.

MAP-OMP on MNIST handwritten images⁵. Here, *iterations* on the horizontal axis of each graph denotes the total iterations where the adaptive MRF framework is performed at the outer-loop, and the signal recovery is performed at the inner-loop. It is clear that Adaptive-MRF takes much less iterations to converge. Note that there are three ripples on the runtime and accuracy curves of both Adaptive-MRF and Adaptive-MAP-OMP according to the setting to run the outer-loop for 3 times. The ripples of Adaptive-Gibbs cannot be seen because it converges much slower (at around 2000 iterations). The ending of each ripple does not appear as a sharp vertical drop because they are resulted from averaging over 10 images. As Adaptive-MRF converges the fastest, this result agrees with its efficient runtime performance.

H. Performance evaluation

In this section, we compare the performance of the proposed Adaptive-MRF with several state-of-the-art CS methods. We evaluate the performance of our Adaptive-MRF over 3 datasets: (1). ten MNIST handwritten digits which are intrinsically sparse; (2). ten CMU-IBD face images in PCA domain; and (3). ten CIFAR-10 natural images in wavelet domain. The compression is performed on these sparse signals. Then, all methods are conducted to recover each image from a few linear measurements.

1) Compressibility.

To demonstrate the compressibility performance of the proposed Adaptive MRF, we evaluate the recovery performance across different sampling rates (M/N). Figure 12 shows the average PSNR curves across different sampling rates on the three datasets, when the noise level (SNR) is 30 dB. Adaptive-MRF offers the highest performance in most cases which indicates that the adaptive MRF provides a good prior to improve sparse signal recovery given a few measurements. When the sampling rate is higher than 0.25, it exceeds other competitors by at least 1 dB on MNIST dataset, 0.5 dB on CMU-IBD dataset, and 1 dB on CIFAR-10 dataset.

To further demonstrate the superior performance of the proposed Adaptive-MRF, we show the visual results of a

⁵The results on CMU-IBD and CIFAR-10 datasets are provided in Section I-C of the supplementary material, and consistent with the result in the main paper

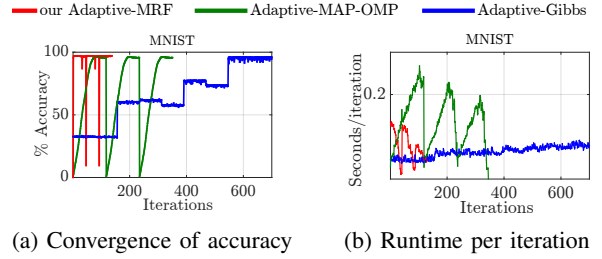


Fig. 11: Solving Eq. (11) (our Adaptive-MRF) vs solving Eq. (9) directly (Adaptive-Gibbs and Adaptive-MAP-OMP) in terms of (a) convergence and (b) runtime per iteration on MNIST dataset⁵. The sampling rate is 0.3 and noise level (SNR) is 30 dB.

MNIST handwritten digit image, a CMU-IBD face image, and a CIFAR-10 natural image in Figure 16, Figure 17, and Figure 18, respectively. Adaptive-MRF gives rise to the best results which contain more details and less noise than its competitors. The full visual results are provided in Section II in the supplementary material document.

2) Noise Tolerance.

To demonstrate the noise tolerance performance, we test the performance of Adaptive-MRF across different noise levels (in SNR). Figure 13 provides the average PSNR curves across different noise levels (SNR) on the three datasets, when the sampling rate is set to 0.3. Adaptive-MRF achieves the best performance in most cases. This indicates that the adaptive MRF provides a good prior to help identify signal information from noisy measurements. Adaptive-MRF outperforms other competitors by at least 2 dB when SNR is higher than 5 dB on MNIST images. It also achieves the best performance in most cases on CMU-IBD face images and CIFAR-10 natural images. However, because the accuracy of an updated MRF is based on the previously estimated sparse signal, Adaptive-MRF performance can be interfered by a certain level of noise. For example, when SNR is low (≤ 15 dB), Adaptive-MRF is beaten by RLPHCS and OMP that do not exploit any signal structure, especially for these two datasets. This could be because the signal representation of CMU-IBD and CIFAR-10 images contains more non-zero coefficients than MNIST images that are strictly sparse. Thus, more error can be accumulated in the estimated signal coefficients; thus, this leads to the inaccurate estimate of the MRF. Nevertheless, when SNR becomes higher (> 15 dB), the measurements contain less noise; thus, the MRF estimation becomes more accurate. Adaptive-MRF outperforms RLPHCS and OMP.

3) Computational Cost.

In this section, we study the computational cost of the proposed Adaptive-MRF in comparison with the competitors from observing the runtime performance across different sampling rate (M/N) and the sparsity levels (k). Figure 14 provides runtime performance at different sampling rates (M/N) on the three datasets when noise level (in SNR) is 30 dB. Figure 15 shows runtime performance at different sparsity levels (k) when the sampling rate and noise level

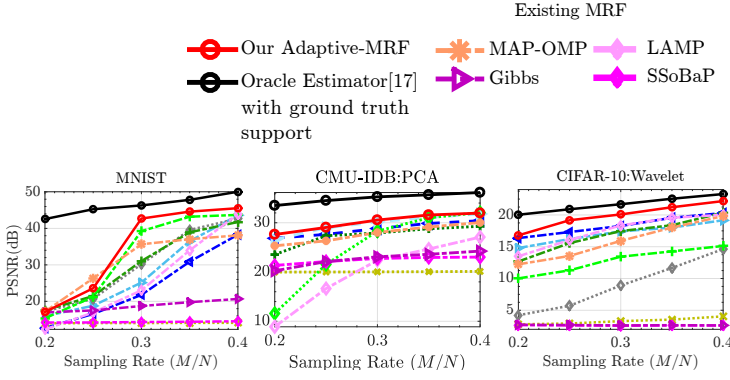


Fig. 12: Compressibility. The PSNR curves across different sampling rates on three datasets at noise level (SNR) of 30 dB.

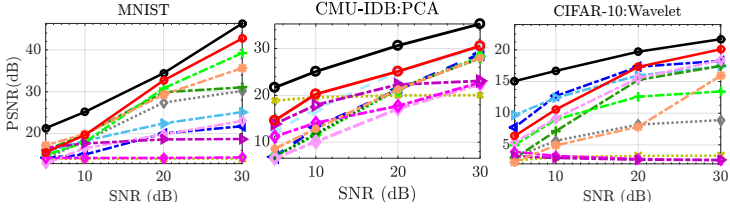


Fig. 13: Noise Tolerance. The PSNR curves across different noise levels (SNR) on three datasets at sampling rate of 0.3.

are 0.3 and 30 dB, respectively. Adaptive-MRF shows to require a moderate runtime which is stable across different sampling rates and sparsity levels. In the experiment on MNIST handwritten images, the average runtime of our Adaptive-MRF is faster than MAP-OMP, StructOMP, and Gibbs, but slower than some algorithms that exploit signal structure—Pairwise MRF, LAMP, MBCS-LBP, SSoBaP, and GCoSAMP. For PCA signals of CMU-IDB images, our approach is faster than MAP-OMP, Gibbs, SSoBaP, MBCS-LBP, and StructOMP; however, it is slower than Pairwise MRF, LAMP, GCoSAMP, OMP, and RLPHCS. For wavelet signals of CIFAR-10 datasets, our Adaptive-MRF is faster than MAP-OMP, Gibbs, SSoBaP, MBCS-LBP, and StructOMP; is comparable to Pairwise MRF; and is slower than LAMP, GCoSAMP, OMP, and RLPHCS. Note that OMP and RLPHCS require less computation because they do not exploit signal structure. SSoBaP has a small runtime only with MNIST handwritten images, which could be because the algorithm converges before reaching an optimal value, as it provides poor accuracy. LAMP performs very fast because it exploits a graph cut method in estimating the support; however, its accuracy is very low. GCoSAMP is a fast algorithms that relies on a geometric assumption of signal structure, but the accuracy is much lower.

V. CONCLUSION

We propose a novel graphical compressive sensing model to better capture the structure of sparse signals. Through imposing a graphical sparsity prior on the sparse signal, and adjusting all involved model parameters according to the observed measurements with a newly developed adaptive MRF inference framework, our model exhibits two important qualities in representing the structure of sparse signal, namely

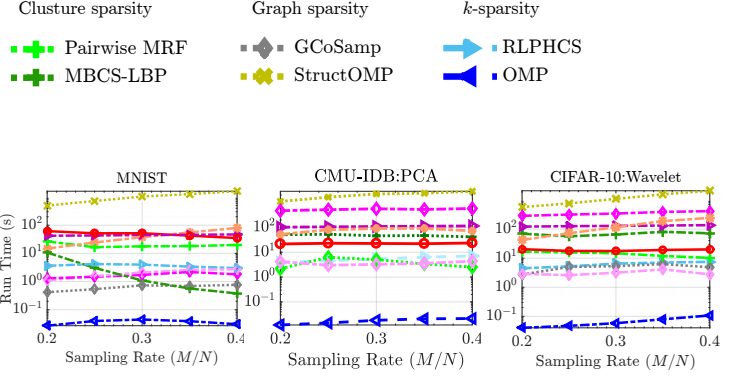


Fig. 14: Computational Cost. Runtime curves across different sampling rates on three datasets at noise level (SNR) of 30 dB.

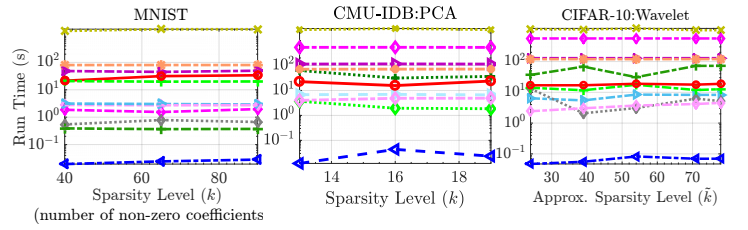


Fig. 15: Computational Cost. Runtime curves across different sparsity levels on three datasets under the sampling rate of 0.4 and noise level of 30 dB.

generality and adaptability. Experiments on three real-world datasets reveal that our model outperforms the state-of-the-art competitors in recovery accuracy and noise tolerance with stable runtime across different sampling rates and signal sparsity.

APPENDIX A

DERIVATION OF THE SUB-OPTIMIZATION PROBLEMS

A. Optimization over s

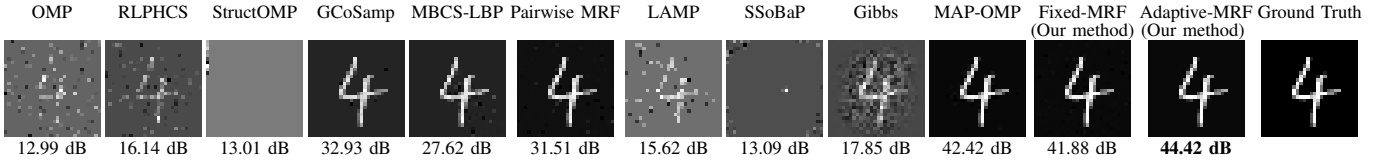
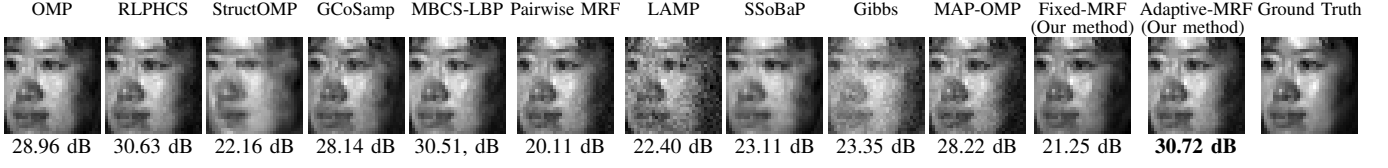
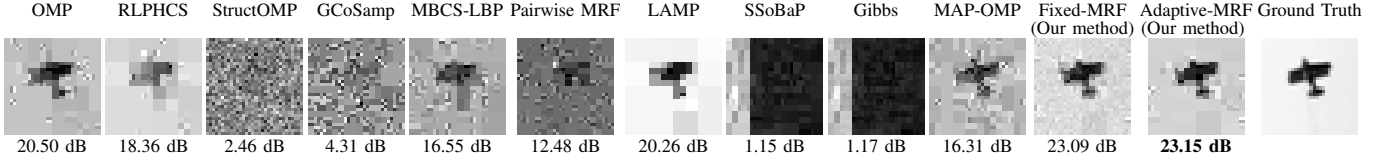
In this section, we provide derivation to Eq.(14). From the optimization problem Eq. (13), given x , σ_n , and $\Sigma_{x,s}$, the optimization problem over s is

$$\begin{aligned} \min_s \quad & \frac{1}{2\sigma_n} x_s^T A_s^T A_s x_s - \frac{1}{\sigma_n} y^T A_s x_s + \frac{1}{2} x_s^T \Sigma_{x,s}^{-1} x_s \\ & + \frac{1}{2} \log |\sigma_n I + A_s \Sigma_{x,s} A_s^T| - \log p(s; \hat{\Theta}_{\hat{G}}) \end{aligned} \quad (26)$$

Let $v \in \{0, 1\}^N$ be a binary variable vector that is the result from mapping each coefficient of s to binary value 0 and 1, i.e., if $s_i > 0$, then $v_i = 1$; otherwise, $v_i = 0$. We exploit Hadamard product properties to extract v by transforming the following terms:

$$\begin{aligned} x_s^T A_s^T A_s x_s &= (x \odot v)^T A^T A (x \odot v) = v^T X^T A^T A X v \\ x_s^T \Sigma_{x,s}^{-1} x_s &= (x \odot v)^T \Sigma_x^{-1} (x \odot v) = v^T X^T \Sigma_x^{-1} X v. \\ \frac{1}{\sigma_n} y^T A_s x_s &= \frac{1}{\sigma_n} y^T A (x \odot v) = \frac{1}{\sigma_n} y^T A X v. \end{aligned} \quad (27)$$

The fourth term in Eq. (26) can be approximated with summation of the logarithm of determinant of diagonal entries

Fig. 16: Visual results of some selected MNIST digit images (at $M/N = 0.3$, $\text{SNR} = 30$ dB).Fig. 17: Visual results of a selected CMU-DB face images from wavelet signal reconstruction (at $M/N = 0.3$, $\text{SNR} = 30$ dB).Fig. 18: Visual results of a selected CIFAR-10 images from wavelet signal reconstruction (at $M/N = 0.3$, $\text{SNR} = 30$ dB).

in $(\sigma_n \mathbf{I} + \mathbf{A}_s \Sigma_{x,s} \mathbf{A}_s^T)$ that is positive definite:

$$\log |\sigma_n \mathbf{I} + \mathbf{A}_s \Sigma_{x,s} \mathbf{A}_s^T| \leq \sum_{i \in \mathcal{V}} \log [\Sigma_x]_{i,i} + \log [(\sigma_n \Sigma_{x,s}^{-1} + \mathbf{A}_s^T \mathbf{A}_s)]_{i,i}, \quad (28)$$

where \mathcal{V} is the set of nodes, and each node is mapped from each coefficient in \mathbf{v} . The notation $[\Sigma_x]_{i,i}$ refers to the i -th diagonal entry of the matrix Σ_x , and $[(\sigma_n \Sigma_{x,s}^{-1} + \mathbf{A}_s^T \mathbf{A}_s)]_{i,i}$ denotes to the i -th diagonal entry of the matrix $(\sigma_n \Sigma_{x,s}^{-1} + \mathbf{A}_s^T \mathbf{A}_s)$. We decompose \mathbf{v} from this term as follows:

$$\sum_{i \in \mathcal{V}} \log [(\sigma_n \Sigma_{x,s}^{-1} + \mathbf{A}_s^T \mathbf{A}_s)]_{i,i} \approx \sum_{i=1}^N v_i \log [(\sigma_n \Sigma_x^{-1} + \mathbf{V}' \mathbf{A}^T \mathbf{A} \mathbf{V}')]_{i,i}, \quad (29)$$

where \mathbf{V} and \mathbf{V}' are the diagonal matrices whose diagonal entries are the current and the previous estimation of \mathbf{v} . Substitute Eq. (29) into Eq. 28, we obtain

$$\log |\sigma_n \mathbf{I} + \mathbf{A}_s \Sigma_{x,s} \mathbf{A}_s^T| \leq \sum_{i=1}^N v_i \log [\Sigma_x]_{i,i} + \sum_{i=1}^N v_i \log [(\sigma_n \Sigma_x^{-1} + \mathbf{V}' \mathbf{A}^T \mathbf{A} \mathbf{V}')]_{i,i}, \quad (30)$$

Combining all the transformations Eq. (27) and Eq. (30), we obtain the MAP problem as in Eq.(14).

B. Optimization over σ_n

In this section, we provide derivation of the update formulation Eq. (19) for σ_n . From the sub-optimization over σ_n Eq.(18). Let $\lambda = \sigma_n \mathbf{1}$ be a vector where each element is noise variance σ_n . Given $\Sigma_{x,s}$, \mathbf{x} , and \mathbf{s} , the optimization Eq.(18) is reformulated as

$$\min_{\lambda} \frac{1}{2\sigma_n} \|\mathbf{y} - \mathbf{A}_s \mathbf{x}_s\|^2 + \frac{1}{2} \log |\mathbf{diag}\{\lambda\} + \mathbf{A}_s \Sigma_{x,s} \mathbf{A}_s^T|. \quad (31)$$

The concave function $h(\lambda) = \log |\mathbf{diag}\{\lambda\} + \mathbf{A}_s \Sigma_{x,s} \mathbf{A}_s^T|$ is transformed into a convex function which is its upper bound,

using a conjugate function. Let $h^*(\lambda)$ be the concave conjugate function of $h(\lambda)$ as follows:

$$h(\lambda) = \log |\mathbf{diag}\{\lambda\} + \mathbf{A}_s \Sigma_{x,s} \mathbf{A}_s^T| \leq \eta^T \lambda - h^*(\lambda), \forall \eta \geq 0. \quad (32)$$

The equation (32) holds when

$$\eta_k = \nabla_{\lambda_k} \log |\mathbf{diag}\{\lambda\} + \mathbf{A}_s \Sigma_{x,s} \mathbf{A}_s^T| = \text{Tr} \left[\mathbf{e}_k^T (\mathbf{diag}\{\lambda\} + \mathbf{A}_s \Sigma_{x,s} \mathbf{A}_s^T)^{-1} \mathbf{e}_k \right]. \quad (33)$$

Thus, we have $\eta = \mathbf{diag}\{(\mathbf{diag}\{\lambda\} + \mathbf{A}_s \Sigma_{x,s} \mathbf{A}_s^T)^{-1}\}$.

Substituting (32) into (31), we obtain the following reformulated sub-problem over σ_n :

$$\min_{\lambda} \frac{1}{\sigma_n} (\mathbf{y} - \mathbf{A}_s \mathbf{x}_s)^T (\mathbf{y} - \mathbf{A}_s \mathbf{x}_s) + \eta^T \lambda = \sum_{i=1}^M \left(\frac{d_i^2}{\lambda_i} + \lambda_i \eta_i \right), \quad (34)$$

where d_i denotes the i -th entry of $\mathbf{d} = \mathbf{y} - \mathbf{A}_s \mathbf{x}_s$. Because $\lambda > 0$, we obtain $\lambda_i^{new} = \sqrt{\frac{d_i^2}{\eta_i}}$. Thus, $\sigma_n^{new} = \frac{1}{M} \sum_{i=1}^M \sqrt{\frac{d_i^2}{\eta_i}}$.

C. Optimization over $\Sigma_{x,s}$

In this section, we provide derivation of the update formulation Eq. (21) for $\Sigma_{x,s}$. From the sub-optimization over Σ_x Eq. (20), we let ν be a vector of the diagonal entry in Σ_x . Given \mathbf{x} , \mathbf{s} , and σ_n , we have the following optimization problem over Σ_x

$$\min_{\nu} \frac{1}{2} \mathbf{x}^T \Sigma_x^{-1} \mathbf{x} + \frac{1}{2} \log |\sigma_n \mathbf{I} + \mathbf{A}' \Sigma_x \mathbf{A}'^T|, \quad (35)$$

where $\mathbf{A}' = \mathbf{A} \mathbf{V}$ is the product between \mathbf{A} and \mathbf{V} to suppress the columns associated with zero elements in \mathbf{x} . The first term in (35) is convex over ν , while the second term is concave over ν . We will transform the second term into a convex function, by, first, decomposing the logarithm term as follows:

$$\log |\sigma_n \mathbf{I} + \mathbf{A}' \Sigma_x \mathbf{A}'^T| = \log |\Sigma_x^{-1}| + \frac{1}{\sigma_n} \mathbf{A}'^T \mathbf{A}' + \log |\sigma_n \mathbf{I}| + \log |\Sigma_x|. \quad (36)$$

Let β be a point-wise inverse of the vector ν , i.e., $\beta = \nu^{\odot -1}$. We use a conjugate function to find a strict upper bound of the

concave function $g(\beta) = \log |\Sigma_x^{-1} + \frac{1}{\sigma_n} \mathbf{A}'^T \mathbf{A}'|$, as follows, $\forall \alpha \geq 0$,

$$g(\beta) \leq \alpha^T \beta - g^*(\beta), \quad (37)$$

where $g^*(\beta)$ is the concave conjugate function of $g(\beta)$ and $\alpha = [\alpha_1, \dots, \alpha_K]^T$. The equation (37) holds when

$$\begin{aligned} \alpha_k &= \nabla_{\beta_k} \log |\Sigma_x^{-1} + \frac{1}{\sigma_n} \mathbf{A}'^T \mathbf{A}'| \\ &= \text{Tr} \left[\mathbf{e}_k^T (\Sigma_x^{-1} + \frac{1}{\sigma_n} \mathbf{A}'^T \mathbf{A}')^{-1} \mathbf{e}_k \right]. \end{aligned} \quad (38)$$

Thus, $\alpha = \text{diag}\{(\Sigma_x^{-1} + \frac{1}{\sigma_n} \mathbf{A}'^T \mathbf{A}')^{-1}\}$. Substituting (37) into (35) and using Eq(36), we have the subproblem as follows:

$$\begin{aligned} \min_{\nu} \mathbf{x}^T \Sigma_x^{-1} \mathbf{x} + \alpha^T \beta + \log |\Sigma_x| = \\ \sum_{i=1}^N ((x_i^2 + \alpha_i) \nu_i^{-1} + \log \nu_i). \end{aligned} \quad (39)$$

Because $\nu_i > 0$, the update of ν_i is $\nu_i^{\text{new}} = x_i^2 + \alpha_i$.

REFERENCES

- [1] D. L. Donoho, "Compressed sensing," *IEEE Trans. Inform. Theory*, vol. 52, no. 4, pp. 1289–1306, 2006.
- [2] R. G. Baraniuk, V. Cevher, M. F. Duarte, and C. Hegde, "Model-based compressive sensing," *IEEE Trans. Inform. Theory*, vol. 56, no. 4, pp. 1982–2001, April 2010.
- [3] R. G. Baraniuk, V. Cevher, and M. B. Wakin, "Low-dimensional models for dimensionality reduction and signal recovery: A geometric perspective," *Proceedings of the IEEE*, vol. 98, no. 6, pp. 959–971, 2010.
- [4] J. Huang, T. Zhang, and D. Metaxas, "Learning with structured sparsity," *JMLR*, vol. 12, no. Nov, pp. 3371–3412, 2011.
- [5] M. Yuan and Y. Lin, "Model selection and estimation in regression with grouped variables," *Journal of the Royal Statistical Society: Series B (Statistical Methodology)*, vol. 68, no. 1, pp. 49–67, 2006.
- [6] Y. C. Eldar and M. Mishali, "Robust recovery of signals from a structured union of subspaces," *IEEE Trans. Inform. Theory*, vol. 55, no. 11, pp. 5302–5316, Nov 2009.
- [7] M. S. Crouse, R. D. Nowak, and R. G. Baraniuk, "Wavelet-based statistical signal processing using hidden markov models," *IEEE Trans. Signal Processing*, vol. 46, no. 4, pp. 886–902, Apr 1998.
- [8] C. La and M. N. Do, "Tree-based orthogonal matching pursuit algorithm for signal reconstruction," in *2006 ICIP*. IEEE, 2006, pp. 1277–1280.
- [9] L. He and L. Carin, "Exploiting structure in wavelet-based bayesian compressive sensing," *IEEE Trans. Signal Processing*, vol. 57, no. 9, pp. 3488–3497, Sept 2009.
- [10] M. Kowalski and B. Torr sani, "Structured sparsity: from mixed norms to structured shrinkage," in *SPARS'09-Signal Processing with Adaptive Sparse Structured Representations*, 2009.
- [11] C. Hegde, P. Indyk, and L. Schmidt, "A nearly-linear time framework for graph-structured sparsity," in *ICML-15*, 2015, pp. 928–937.
- [12] B. Zhou and F. Chen, "Graph-structured sparse optimization for connected subgraph detection," in *2016 ICDM*. IEEE, 2016, pp. 709–718.
- [13] P. J. Wolfe, S. J. Godsill, and W. Ng, "Bayesian variable selection and regularization for time frequency surface estimation," *Journal of the Royal Statistical Society: Series B (Statistical Methodology)*, vol. 66, no. 3, pp. 575–589, 2004.
- [14] P. Garrigues and B. A. Olshausen, "Learning horizontal connections in a sparse coding model of natural images," in *Advances in Neural Information Processing Systems*, 2008, pp. 505–512.
- [15] V. Cevher, M. F. Duarte, C. Hegde, and R. Baraniuk, "Sparse signal recovery using markov random fields," in *Advances in Neural Information Processing Systems*, 2009, pp. 257–264.
- [16] A. Dr lmeau, C. Herzet, and L. Daudet, "Boltzmann machine and mean-field approximation for structured sparse decompositions," *IEEE Trans. Signal Processing*, vol. 60, no. 7, pp. 3425–3438, 2012.
- [17] T. Peleg, Y. C. Eldar, and M. Elad, "Exploiting statistical dependencies in sparse representations for signal recovery," *IEEE Trans. Signal Processing*, vol. 60, no. 5, pp. 2286–2303, 2012.
- [18] L. Yu, C. Wei, J. Jia, and H. Sun, "Compressive sensing for cluster structured sparse signals: Variational bayes approach," *IET Signal Processing*, vol. 10, no. 7, pp. 770–779, 2016.
- [19] L. Yu, H. Sun, J.-P. Barbot, and G. Zheng, "Bayesian compressive sensing for cluster structured sparse signals," *Signal Processing*, vol. 92, no. 1, pp. 259–269, 2012.
- [20] L. Yu, H. Sun, G. Zheng, and J. P. Barbot, "Model based bayesian compressive sensing via local beta process," *Signal Processing*, vol. 108, pp. 259–271, 2015.
- [21] J. Fang, Y. Shen, H. Li, and P. Wang, "Pattern-coupled sparse bayesian learning for recovery of block-sparse signals," *IEEE Trans. Signal Processing*, vol. 63, no. 2, pp. 360–372, Jan 2015.
- [22] L. Wang, L. Zhao, G. Bi, and C. Wan, "Sparse representation-based isar imaging using markov random fields," *IEEE Journal of Selected Topics in Applied Earth Observations and Remote Sensing*, vol. 8, no. 8, pp. 3941–3953, Aug 2015.
- [23] J. Fang, L. Zhang, and H. Li, "Two-dimensional pattern-coupled sparse bayesian learning via generalized approximate message passing," *IEEE Trans. Image Processing*, vol. 25, no. 6, pp. 2920–2930, June 2016.
- [24] D. P. Wipf, B. D. Rao, and S. Nagarajan, "Latent variable bayesian models for promoting sparsity," *IEEE Trans. Inform. Theory*, vol. 57, no. 9, pp. 6236–6255, Sept 2011.
- [25] L. Zhang, W. Wei, C. Tian, F. Li, and Y. Zhang, "Exploring structured sparsity by a reweighted laplace prior for hyperspectral compressive sensing," *IEEE Trans. Image Processing*, vol. 25, no. 10, pp. 4974–4988, Oct 2016.
- [26] P. Zhao, G. Rocha, and B. Yu, "The composite absolute penalties family for grouped and hierarchical variable selection," *The Annals of Statistics*, pp. 3468–3497, 2009.
- [27] C. Hegde, P. Indyk, and L. Schmidt, "Approximation algorithms for model-based compressive sensing," *IEEE Trans. Inform. Theory*, vol. 61, no. 9, pp. 5129–5147, 2015.
- [28] S. Som and P. Schniter, "Compressive imaging using approximate message passing and a markov-tree prior," *IEEE Trans. Signal Processing*, vol. 60, no. 7, pp. 3439–3448, July 2012.
- [29] J. Ren, J. Liu, and Z. Guo, "Context-aware sparse decomposition for image denoising and super-resolution," *IEEE Trans. Image Processing*, vol. 22, no. 4, pp. 1456–1469, April 2013.
- [30] D. Koller and N. Friedman, *Probabilistic graphical models: principles and techniques*, 2009.
- [31] M. J. Wainwright and M. I. Jordan, "Graphical models, exponential families, and variational inference," *Foundations and Trends® in Machine Learning*, vol. 1, no. 1-2, pp. 1–305, 2008.
- [32] C. Wang, N. Komodakis, and N. Paragios, "Markov random field modeling, inference & learning in computer vision & image understanding: A survey," *Computer Vision and Image Understanding*, vol. 117, no. 11, pp. 1610–1627, 2013.
- [33] S. Parise and M. Welling, "Learning in markov random fields: An empirical study," Citeseer.
- [34] J. Tropp and A. C. Gilbert, "Signal recovery from random measurements via orthogonal matching pursuit," *IEEE Trans. Inform. Theory*, vol. 53, no. 12, pp. 4655–4666, 2007.
- [35] B. D. George and W. Philip, "Decomposition principle for linear programs," *Operations Research*, vol. 8, no. 1, pp. 101–111, 1960. [Online]. Available: <http://www.jstor.org/stable/167547>
- [36] V. Kolmogorov, "Convergent tree-reweighted message passing for energy minimization," *IEEE Trans. Pattern Analysis and Machine Intelligence*, vol. 28, no. 10, pp. 1568–1583, Oct 2006.
- [37] O. Meshi and A. Globerson, "An alternating direction method for dual map lp relaxation," in *Machine Learning and Knowledge Discovery in Databases*. Springer, 2011, pp. 470–483.
- [38] S. Foucart and H. Rauhut, *A mathematical introduction to compressive sensing*, vol. 1, no. 3.
- [39] Z. Zhang, Q. Shi, J. McAuley, W. Wei, Y. Zhang, and A. Van Den Hengel, "Pairwise matching through max-weight bipartite belief propagation," in *2016 CVPR*.
- [40] Y. LeCun, L. Bottou, Y. Bengio, and P. Haffner, "Gradient-based learning applied to document recognition," *Proceedings of the IEEE*, vol. 86, no. 11, pp. 2278–2324, 1998.
- [41] T. Sim, S. Baker, and M. Bsat, "The cmu pose, illumination, and expression database," vol. 25, no. 12, pp. 1615 – 1618, December 2003.
- [42] A. Krizhevsky, "Learning multiple layers of features from tiny images," 2009.